

Thermal conductivity of amorphous and nanocrystalline silicon films prepared by hot-wire chemical-vapor deposition

B. Jugdersuren,¹ B. T. Kearney,² D. R. Queen,² T. H. Metcalf,³ J. C. Culbertson,³ C. N. Chervin,³ R. M. Stroud,³ W. Nemeth,⁴ Q. Wang,⁴ and Xiao Liu^{3,*}

¹*Sotera Defense Solutions, Inc., Herndon, Virginia 20171, USA*

²*NRC Postdoctoral Associate, Naval Research Laboratory, Washington, D.C. 20375, USA*

³*Naval Research Laboratory, Washington, D.C. 20375, USA*

⁴*National Renewable Energy Laboratory, Golden, Colorado 80401, USA*

(Received 7 February 2017; revised manuscript received 26 May 2017; published 31 July 2017)

We report 3ω thermal conductivity measurements of amorphous and nanocrystalline silicon thin films from 85 to 300 K prepared by hot-wire chemical-vapor deposition, where the crystallinity of the films is controlled by the hydrogen dilution during growth. The thermal conductivity of the amorphous silicon film is in agreement with several previous reports of amorphous silicon prepared by a variety of deposition techniques. The thermal conductivity of the as-grown nanocrystalline silicon film is 70% higher and increases 35% more after an anneal at 600 °C. They all have similarly weak temperature dependence. Structural analysis shows that the as-grown nanocrystalline silicon is approximately 60% crystalline, nanograins and grain boundaries included. The nanograins, averaging 9.1 nm in diameter in the as-grown film, are embedded in an amorphous matrix. The grain size increases to 9.7 nm upon annealing, accompanied by the disappearance of the amorphous phase. We extend the models of grain boundary scattering of phonons with two different non-Debye dispersion relations to explain our result of nanocrystalline silicon, confirming the strong grain size dependence of heat transport for nanocrystalline materials. However, the similarity in thermal conductivity between amorphous and nanocrystalline silicon suggests the heat transport mechanisms in both structures may not be as dissimilar as we currently understand.

DOI: [10.1103/PhysRevB.96.014206](https://doi.org/10.1103/PhysRevB.96.014206)

I. INTRODUCTION

The effort to gain a fundamental understanding of thermal transport in amorphous silicon (*a*-Si) and nanocrystalline silicon (nc-Si) has garnered much attention both experimentally [1–11] and theoretically [12–22]. While low thermal conductivity is a prerequisite for possible implementation of nc-Si in thermoelectric applications [10], *a*-Si based electronic devices, such as solar cells and displays, can benefit from improved thermal conduction [23]. Experiments show that the thermal conductivity of nc-Si can be reduced by orders of magnitude from that of its single crystalline form due to strong phonon scattering at grain boundaries [9–11]. However, the low thermal conductivity in almost all *a*-Si originates from strong phonon scattering by local disorder, the origin of which is still unknown [12–18].

The model of minimum thermal conductivity, κ_{\min} , can be used to describe the lowest possible thermal conductivity of all amorphous solids by assuming that the phonon mean free path (MFP) is on the order of either their wavelength or atomic spacing [24]. The κ_{\min} of a given material is often called its amorphous limit. For *a*-Si, a more precise description is given by numerical calculations based on molecular- and lattice-dynamics simulations [12–18]. These calculations work well for most *a*-Si films studied so far, except for a series of hydrogenated *a*-Si films where a 4–6 times higher thermal conductivity has been observed due to improved structural order [4,5]. Computation of molecular and lattice dynamics shows that increased medium-range order improves thermal

conductivity in *a*-Si [16]. Recent research on *a*-Si, both experimental and theoretical, shows that a broad band of vibration modes contributes to heat conduction [6–8,16,17]. While phononlike propagating modes, called propagons, have a MFP ranging from 10 nm to over 1 μm , interactive nonpropagating modes, called diffusons, have a MFP of 10 nm and less. Contribution from high-frequency vibrational modes increases with temperature [8]. In practice, the minimum thermal conductivity has served as a reference lower bound for a given material. However, thermal conductivities lower than κ_{\min} have been experimentally observed in a number of nanostructured crystalline materials [25,26]. These materials show particular promise for use in applications, such as thermoelectric devices and thermal barrier coatings.

Research shows that nanocrystallization is an effective way to reduce thermal conductivity in crystalline silicon [10,27]. Thermal conductivity smaller than the amorphous limit has become achievable in nanocrystalline $\text{Si}_{80}\text{Ge}_{20}$ composites prepared by ball milling with 10-nm-average grain sizes [28] and in multilayered Si/Ge nanodot thin films with layer spacings of 3 nm [27]. Research also shows that nanoparticle inclusion is effective in reducing heat conduction in both amorphous and crystalline materials [22,29–31]. Nanocrystallization has been the preferred approach to make silicon a high-efficiency thermoelectric material [10,28,30,32]. However, a more quantitative insight of heat transport in nc-Si can be obtained if the thermal conductivity of pure nc-Si with varying grain sizes can be studied directly. Wang *et al.* reported such a study in which the average grain sizes were varied from 550 to 76 nm [11]. Using the Born–von Karman (BvK) dispersion relation, they explained their thermal conductivity results by frequency dependent phonon grain boundary scattering, in

*xiao.liu@nrl.navy.mil

addition to impurity and Umklapp scattering, with a single set of parameters, where the only variable is the grain size. It is not clear if such a frequency and grain size dependent phonon scattering mechanism would still be adequate for smaller grain sizes. Feser *et al.* measured the thermal conductivity of nanocrystalline CdSe with average grain sizes between 3 and 6 nm [26]. Using a Morelli-Callaway (MC) dispersion relation, the authors explained their results with a frequency independent phonon grain boundary scattering. Similar to Wang *et al.*, grain size is the only variable. The difference is that their grain sizes are one order of magnitude smaller and their thermal conductivity values are well below κ_{\min} . It would be helpful to bridge the current gap in grain sizes, in particular in nc-Si, and to explain grain size dependent thermal conductivity with a unified theoretical model.

Regardless of the phonon scattering mechanisms, another challenge in nanoscale heat transport in crystalline solids is to understand whether our description of phonons as elastic waves can remain valid for nanostructured materials as their thermal conductivity has been reduced close to or below the amorphous limit. Numerical calculations show that in *a*-Si, phonon velocities and wave vectors are not well defined and heat is transported diffusively by coupling of extended vibration modes [12,14,18,33]. It is not clear if the concepts of propagon, diffuson, and locon developed specifically for amorphous solids [15] are also appropriate for nanostructured crystalline solids. A transition from propagating to diffusive heat transport may take place in nc-Si as grain size decreases.

In the present paper, we report the thermal conductivity, κ , of amorphous and nanocrystalline silicon thin films from 80 to 300 K. For the nc-Si film, κ was measured before and after annealing at 600°C. The data of κ of fully amorphous, 60% nanocrystalline, and fully nanocrystalline silicon are compared with results of previously published grain size dependent thermal conductivity measurements [11,26]. Our results not only provide κ at the 10-nm grain size range, bridging the gap from the previous studies, but also provide a unified description of grain size dependent thermal conductivity for nc-Si. In addition, the similarity in κ , both in magnitude and temperature dependence, between *a*-Si and nc-Si at the 10-nm grain size range suggests a similarly weak temperature-dependent heat transport mechanism in both structures.

II. EXPERIMENT

Both *a*-Si and nc-Si films were deposited by hot-wire chemical-vapor deposition (HWCVD) at the National Renewable Energy Laboratory (NREL). Film growth conditions were similar to those used in several previous studies [34–37]. Substrate temperature was kept at 250°C with background pressure in the low 10^{-7} Torr, filament temperature of 1700°C, and gas pressure at 25 mTorr for all depositions. Sapphire substrates were used for 3ω thermal conductivity measurements, and silica substrates were used for structural characterizations. Silane (SiH_4) gas flow was maintained at 8 SCCM, where SCCM denotes cubic centimeter per minute at STP, and the hydrogen (H_2) flow rate was varied to reach the desired dilution molar ratio $R = \text{H}_2/\text{SiH}_4$, which determines the crystallinity of the films. It has been known that, as H_2 dilution increases, a transition from an amorphous to a

nanocrystalline phase takes place at $R \approx 3$ [34]. The *a*-Si and nc-Si films used in this paper have $R = 1$ and 8; and the film thicknesses are 0.60 and 0.59 μm with deposition rates of 0.28 and 0.42 nm/s, respectively. Film thickness was measured with different N&K Spectrophotometers at both NREL and Naval Research Laboratory. The results agree to within 10%, which is one of the main sources of error in the thermal conductivity evaluation. According to Han *et al.* [35], our *a*-Si and nc-Si films should have a hydrogen content of 13 and 4 at. %, respectively. However, as the deposition rate of our *a*-Si is lower than that of the $R = 1$ film in Ref. [35], we expect that the hydrogen content in our *a*-Si is also lower. Technically, the as-grown *a*-Si and nc-Si should be called hydrogenated *a*-Si and nc-Si, or *a*-Si:H and nc-Si:H, due to hydrogen passivation of defect states. The same is true for the other HWCVD *a*-Si films mentioned below. For convenience, we will drop “hydrogenated” in this paper. The as-grown nc-Si films were furnace annealed in a vacuum of 2×10^{-6} Torr, first to 250°C for 3 h with a ramp-up rate of 1°C/min for hydrogen effusion without explosive evolution and then to 600°C for another 2 h with a rate of 5°C/min to fully crystallize the amorphous regions in the film.

Cross sections of the *a*-Si and nc-Si samples were prepared by *in situ* focused ion-beam (FIB) liftout with an FEI Nova 600 FIB scanning electron microscope. Transmission electron microscopy (TEM) studies were performed with a JEOL 2200FS 200-keV field emission TEM, equipped with a Noran System Six energy dispersive spectroscopy system, and Gatan UltraScan 1000 CCD. Grazing-incidence x-ray-diffraction (XRD) measurements of the Si films were collected with a Rigaku SmartLab x-ray diffractometer using fixed $\text{CuK}\alpha$ radiation in parallel-beam mode. The angle of incidence was set to 0.5° and the detector was rotated to measure from 20° to 70° in increments of 0.02° and counts were accumulated for 1 s at each step. Sample height alignment was conducted via Rigaku’s automated height-alignment function for flat samples. The Raman spectra were acquired with a home-built confocal micro-Raman setup composed of a 0.5-m single spectrometer using a 1800-groove/mm grating; a liquid nitrogen cooled back-thinned/deep-depleted CCD sensitive in the visible-near IR spectral range; and a single-mode 488-nm laser with typical spot size $< 1 \mu\text{m}$ and intensity $\sim 0.5 \text{ mW}$ at the sample.

Figures 1(a) and 1(b) show the images of a cross-sectional TEM and fast Fourier-transform (FFT) diffractogram of the *a*-Si and nc-Si films, respectively, grown at the same time on companion silica substrates. The TEM image of *a*-Si shows a uniform amorphous structure. No evidence for long-range crystalline order is observed in the TEM image, diffractogram, or selected area electron diffraction from the *a*-Si sample. However, a greater degree of short-range order at length scales up to 1 nm in the *a*-Si film, compared to the amorphous silica substrate, can be inferred from the moderately sharper rings observed for the selected area electron diffraction patterns from the film compared to those from the substrate (not shown). For nc-Si, the atomic lattice planes are resolved due to its crystalline structure. The corresponding lattice spacings are labeled on the FFT diffractogram in the inset. Figure 1(c) shows a TEM image of the nc-Si film covering the whole thickness, revealing a columnar growth pattern in the nanocrystalline region and a $\sim 100\text{-nm}$ -thick incubation

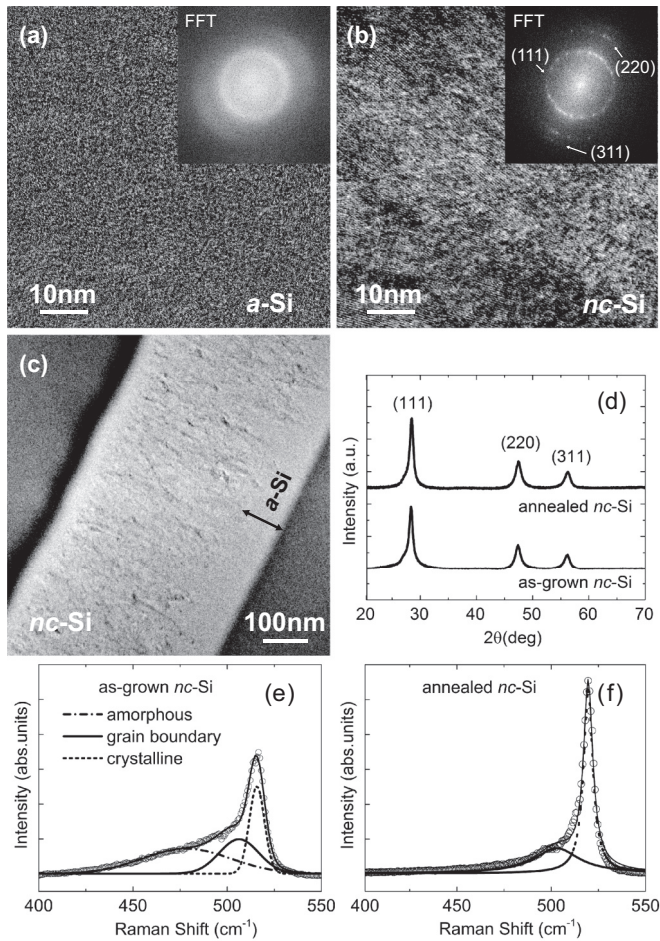


FIG. 1. (a), (b) Cross-sectional transmission electron microscope images of as-grown *a*-Si:H and *nc*-Si:H films. The inserts are the FFT diffractogram of the same films, where the resolved lattice spacings are labeled. (c) The cross-sectional transmission electron microscope image of the as-grown *nc*-Si:H film over the entire thickness range that includes the substrate and capping layer. The *a*-Si incubation layer is indicated. (d) XRD spectra of *nc*-Si films: as grown and annealed at 600 °C. (e), (f) Raman spectra of *nc*-Si film: as grown and annealed at 600 °C.

amorphous layer right above the substrate, both of which are typical for HWCVD *nc*-Si films. Figure 1(d) shows the x-ray-diffraction spectra of the *nc*-Si film before and after annealing, where the average grain sizes, 9.1 and 9.7 nm, respectively, are calculated from the three most visible diffraction peaks associated with planes of (111), (220), and (311) using the Scherrer equation. The peaks index with the (111), (220), and (311) reflections of Si (ICDD no. 0-026-1481). The grain size for the as-grown *nc*-Si is consistent with the TEM image shown in Fig. 1(b). The slight grain growth upon annealing can be understood as the incorporation of the amorphous region into individual grains with minimal merging of grains. The Raman spectra for the as-grown and the annealed *nc*-Si films are shown in Figs. 1(e) and 1(f), respectively. The spectra can be deconvoluted and fitted with three Gaussian peaks originating from amorphous, crystalline, and grain boundary phases centered at 480, 520, and 494–507 cm^{-1} , respectively. The crystalline volume fraction is estimated from the ratio of

the integrated intensity of both crystalline and grain boundary peaks to the total intensity, taking into account the grain size dependent scattering cross-section ratio between amorphous and crystalline phases [38]. We find that the as-grown *nc*-Si film is 60% crystalline and has become 100% after annealing. With additional laser transmission experiments, we also estimate that the incubation *a*-Si layer in the as-grown film contributes less than 3% to the total Raman spectra and has no effect on our analysis. Still, the crystalline volume fraction of the as-grown film is lower than those films with similar *R* prepared at NREL [34,35], presumably due to the smaller thickness of our film. For the annealed film, we see no sign of a Raman peak at 480 cm^{-1} from an amorphous phase, confirming its fully crystalline nature as expected from the solid phase crystallization of *a*-Si [39].

The differential 3ω method is used to measure κ of these films; the experimental design was similar to that used by Cahill and coworkers [2,40]. A planar metal line, made of 5-nm Ti and 120-nm Au, is deposited directly on either the *a*-Si or *nc*-Si thin film by a photolithography and liftoff process. This metal line, 1.20 mm long and 10 μm wide, acts as both a heater and a thermometer which probes temperature oscillations in the film generated by an ac current in the frequency range of 3–1500 Hz. Thicknesses of our films are significantly smaller than the heater width, satisfying the one-dimensional heat flow condition of the 3ω technique. To validate accuracy of our 3ω setup, we measured κ of a 0.5- μm -thick *a*-SiO₂ film thermally grown on a Si wafer. The κ of this film is identical to that of a similarly grown 0.99- μm -thick *a*-SiO₂ film [2] over the entire temperature range of this work, 80–300 K.

III. RESULTS

The experimental data of κ versus temperature T of HWCVD *a*-Si and *nc*-Si thin films are shown in Figs. 2(a) and 2(b), together with some of the published results in the same temperature range for comparison. The dominant phonon wavelength $\lambda_{\text{dom}} = v_s/v_{\text{dom}}$ for heat transport is shown on the top x axis, where $v_s = 6084$ m/s is the average sound velocity [11] and the dominant heat carrying phonon frequency $\nu_{\text{dom}} = 90$ [GHz K⁻¹] T [41].

Figure 2(a) compares κ of our *a*-Si to other depositions and models. The data of our HWCVD *a*-Si agree with those of a 0.52- μm -thick sputtered *a*-Si with 1-at. % hydrogen [2] and a 0.13- μm -thick electron-beam evaporated *a*-Si without hydrogen [3]. As our *a*-Si should contain more than 1 at. % H, our result confirms that κ of *a*-Si depends only weakly on deposition methods and hydrogen content [2,7]. In fact, most of the published κ of *a*-Si are located within the 1–2-W/mK range and bounded by κ_{min} at the lower end [24].

Thickness and MFP dependent thermal conductivity studies show thicker films would have higher κ [6–8]. The theory of minimum thermal conductivity gives this lower limit by assuming atoms or groups of atoms vibrate with random phases and the phonon MFP is taken as one-half of its wavelength. Numerical results based on the Kubo theory, which uses a specific structural model and a realistic interatomic potential to compute the phonon spectrum, show that the majority of vibration modes are not localized and that heat is transported by the coupling of these modes. However, due to its limited

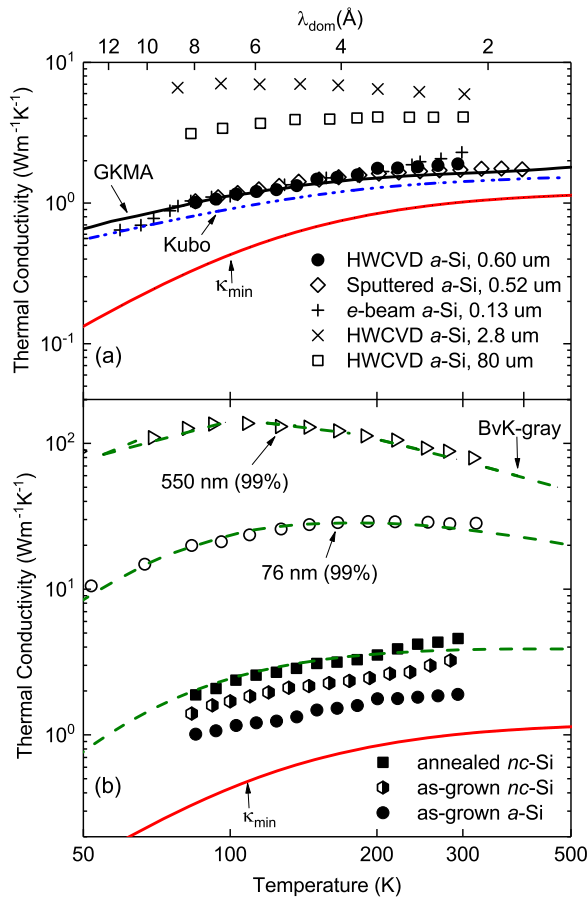


FIG. 2. Thermal conductivity vs temperature. (a) HWCVD *a*-Si film, 0.60 μm thick grown at 250 $^{\circ}\text{C}$, compared with four previously published results of *a*-Si: sputtered, 0.52 μm thick grown at 230 $^{\circ}\text{C}$ [2]; electron-beam evaporated, 0.13 μm thick grown at room temperature [3]; HWCVD, 2.8 μm thick grown at 430 $^{\circ}\text{C}$ [5]; and HWCVD, 80 μm thick grown at 430 $^{\circ}\text{C}$ [4]. Also included are the minimum thermal conductivity κ_{min} of *a*-Si [24], a numerical computation for *a*-Si based on the Kubo theory [14] with contribution from vibration modes with energy less than 10 meV manually added (labeled as Kubo) [2], and a Green-Kubo modal analysis result that naturally contains anharmonic effect and low-energy modes (labeled as GKMA) [18]. (b) All three HWCVD films: *a*-Si, as-grown nc-Si, and annealed nc-Si, compared with two previously published results of nc-Si with grain sizes of 550 and 76 nm [11]. Also included are fitting curves for the three nc-Si using the Born-von Karman dispersion relation and frequency independent (gray) grain boundary scattering, and κ_{min} of *a*-Si.

size, lower frequency modes that are not included in the computation have to be added manually. Such numerical computation gives a more accurate description of κ for *a*-Si [14,15]. One of these theoretical results given in Ref. [2] for a 0.5- μm -thick film is reproduced in Fig. 2(a) together with κ_{min} for comparison. There are a number of variations for numerical computation distinguished by different structural models and/or by choosing whether or not to consider anharmonic effects [3,4,16,17]. Recently, a Green-Kubo modal analysis method has been developed by Lv and Henry to compute each modal contribution to κ without having to define sound velocity [18]. Anharmonicity as well as low-energy modes are

naturally included. Their result for *a*-Si, which is the closest to the experimental data, is also included in Fig. 2(a).

It is interesting to note that the FFT diffractogram in Fig. 1(a) shows improved structural order at length scales up to 1 nm, presumably due to hydrogen dilution, which is known to improve the structural order of *a*-Si [36]. Apparently, such improvement is too short in length scale to affect κ . Much larger structural improvement has been observed in HWCVD *a*-Si deposited at a growth temperature of 430 $^{\circ}\text{C}$ without hydrogen dilution, where κ increases by more than a factor of 2 [4,5], also shown in Fig. 2(a). It is worth mentioning that the 430 $^{\circ}\text{C}$ deposited HWCVD *a*-Si films also have two orders of magnitude lower internal friction at low temperatures [42] than the 250 $^{\circ}\text{C}$ deposited HWCVD *a*-Si films with hydrogen dilution [37]. Lower internal friction means less disorder-induced low-energy excitations to dissipate elastic energy, consistent with higher κ . This comparison shows that higher growth temperature is far more effective than hydrogen dilution in improving structural order in *a*-Si. The median-range structural improvement may be responsible for the improved thermal conduction and reduced elastic energy dissipation of the material; a similar conclusion has recently been drawn in the internal friction study of electron-beam deposited *a*-Si films [43].

Figure 2(b) shows κ of all three HWCVD films. The κ of as-grown nc-Si is 70% higher than that of *a*-Si and increases 35% more after an anneal at 600 $^{\circ}\text{C}$. The as-grown nanocrystalline silicon is approximately 60% nanocrystalline, nanograins and grain boundaries included. The nanograins, averaging 9.1 nm in diameter in the as-grown film, are embedded in an amorphous matrix. In our evaluation of the as-grown nc-Si, we subtract the contribution of the amorphous incubation layer from the measured κ by using the series resistor rule. We assume the incubation layer has the same κ as the *a*-Si film for the entire temperature range. However, as the incubation layer may most likely already contain a significant amount of nanocrystals and undergo a structural transition to the nanocrystalline phase as the film grows thicker, the right amount of correction to κ is unknown and should therefore be less than 10%. The grain size increases to 9.7 nm upon annealing, accompanied by the disappearance of the amorphous phase. Interestingly, although κ more than doubles as nanocrystalline content increases progressively from 0 to 100%, $\kappa(T)$ of all three films maintains a remarkably similar temperature dependence. In amorphous solids, most of the heat is transported by diffusons due to the presence of disorder [14]. Contributions to heat conduction by propagons, the phonon analog in amorphous solids, can still be meaningful in *a*-Si, depending on film thickness and temperature, but not in amorphous SiO_2 [6–8,17]. In contrast, phonon scattering from grain boundaries dominates thermal conductivity in nanocrystalline solids. For comparison, the results of κ of nc-Si with grain sizes of 550 and 76 nm prepared by densification of silicon powder are also shown in Fig. 2(b) [11]. The lower values of κ of our annealed nc-Si with grain size of 9.7 nm can be understood as a consequence of increased grain boundary scattering due to smaller grain sizes. On the other hand, the similarity in κ between amorphous and nanocrystalline silicon suggests the thermal conduction mechanism in nc-Si may not differ from that in *a*-Si in any significant way.

IV. DISCUSSION

To examine if the grain boundary scattering mechanisms used by Wang *et al.* can be extended to nc-Si with grain sizes as small as 10 nm [11], we analyze our thermal conductivity results with the same formula and parameters. The general kinetic expression of κ can be written as

$$\kappa = \frac{1}{3} \sum_{\text{pol}} \int C(\omega, T) v(\omega) \Lambda_{\text{eff}}(\omega, T) d\omega \quad (1)$$

where ω is the angular frequency of phonons; $C(\omega, T)$, $v(\omega)$, and $\Lambda_{\text{eff}}(\omega, T)$ are spectral specific heat, group velocity, and effective MFP of phonons, respectively. Phonon dispersion determines phonon density of states and group velocity. So both $C(\omega, T)$ and $v(\omega)$ depend on the choice of phonon dispersion relation, while $\Lambda_{\text{eff}}(\omega, T)$ depends on the phonon scattering mechanisms. The sum is over three acoustic phonon branches: one longitudinal and two transverse; for simplicity, we use one generic acoustic phonon branch and multiply it by 3 with average sound velocity $v_s = 6084$ m/s [11].

To compare with previous studies, we use three different models of the dispersion relation in this paper. The first is the Debye model, which gives the linear dispersion relation: $\omega = v_s q$, where q is the phonon wave vector. This gives the (Debye) cutoff frequency $\omega_D/2\pi = 11.03$ THz. The linear dispersion relation also determines phonon density of states per volume

$$g(\omega) = \frac{3}{2\pi^2} \frac{\omega^2}{v_s^3} \quad (2)$$

and spectral specific heat

$$C(\omega) = \frac{3k_B^3 T^2}{2\pi^2 v_s^3 \hbar^2} \frac{x^4 e^x}{(e^x - 1)^2}, \quad (3)$$

where k_B denotes the Boltzmann constant, \hbar denotes the reduced Plank constant, and $x = \hbar\omega/k_B T$. It is known that the Debye dispersion overestimates group velocity of high-frequency phonons. However, the Debye thermal conductivity can be simplified to a well-known form as

$$\kappa_D = \frac{k_B v_s}{2\pi^2} \left(\frac{k_B T}{\hbar v_s} \right)^3 \int_0^{x_D} \Lambda_{\text{eff}}(x, T) \frac{x^4 e^x}{(e^x - 1)^2} dx, \quad (4)$$

which gives κ_{min} when $\Lambda_{\text{eff}}(\omega, T) = \pi v_s/\omega$. Therefore, the connection with κ_{min} makes the Debye model useful to compare with the other two models.

The second is the BvK model described in detail by Dames and Chen [44], which gives a more realistic phonon dispersion relation as $\omega = \omega_0 \sin(\pi q/2q_0)$. The BvK dispersion reduces $v(\omega)$ ($=d\omega/dq$) of high-frequency phonons and it resembles the actual phonon dispersion [45]. For ease of comparison, we choose the cutoff wave vector to be the same as the one used in the Debye model $q_0 = \omega_D/v_s$ and the cutoff frequency to be $\omega_0 = 2\omega_D/\pi$, so that $v(\omega)$ remains the same as in the Debye model at low frequencies. For the BvK dispersion relation, we have phonon group velocity

$$v(\omega) = v_s \cos(\pi q/2q_0), \quad (5)$$

phonon density of states

$$g(\omega) = \frac{6q_0^2}{\pi^4 v_s} \frac{[\sin^{-1}(\omega/\omega_0)]^2}{\cos(\pi q/2q_0)}, \quad (6)$$

and spectral specific heat

$$C(\omega) = \frac{6\hbar^2 q_0^2}{\pi^4 k_B T^2 v_s} \frac{\omega^2 e^x [\sin^{-1}(\omega/\omega_0)]^2}{(e^x - 1)^2 \cos(\pi q/2q_0)}. \quad (7)$$

The BvK thermal conductivity becomes

$$\kappa_{\text{BvK}} = \frac{2\hbar^2 q_0^2}{\pi^4 k_B T^2} \int_0^{\omega_0} \Lambda_{\text{eff}}(\omega, T) \frac{\omega^2 e^x [\sin^{-1}(\omega/\omega_0)]^2 d\omega}{(e^x - 1)^2}. \quad (8)$$

The third is the MC model [26], which has a Debye-like linear dispersion at low frequencies and assigns a cutoff for each phonon polarization based on the actual phonon dispersion [45]. For simplicity and ease of comparison, we use the Debye dispersion at low ω and the same cutoff as the BvK model, ω_0 . So κ_{MC} can be determined by Eq. (4) with the upper bound of the integration replaced by $x_0 = \hbar\omega_0/k_B T$. Effectively, the MC model assigns group velocity $v(\omega) = 0$ for $\omega > \omega_0$. An illustrative dispersion relation plot for the three models used in this paper is shown in the inset of Fig. 3(a).

The effective phonon MFP, $\Lambda_{\text{eff}}(\omega, T)$, combines phonon scattering mechanisms such as impurity or defect scattering $\Lambda_I(\omega)$, Umklapp scattering $\Lambda_U(\omega, T)$, and grain boundary scattering $\Lambda_B(\omega)$ by Matthiessen's rule:

$$\Lambda_{\text{eff}}^{-1}(\omega, T) = \Lambda_I^{-1}(\omega) + \Lambda_U^{-1}(\omega, T) + \Lambda_B^{-1}(\omega), \quad (9)$$

where $\Lambda_I^{-1}(\omega) = A_1 \omega^4/v_s$, and $\Lambda_U^{-1}(\omega, T) = B_1 \omega^2 T e^{-B_2/T}/v_s$ [11]; A_1 , B_1 , and B_2 are fitting parameters. Wang *et al.* considered both frequency independent (gray) and frequency dependent (nongray) grain boundary scattering for κ of nc-Si of grain sizes 76 nm and above [11]. For the gray formula, $\Lambda_B(\omega) = \alpha D_{\text{avg}}$; for the nongray formula, $\Lambda_B(\omega) = \alpha D_{\text{avg}}(0.7\omega_0/\omega)$. Here α and D_{avg} in both cases are a fitting parameter and the average grain size, respectively. The factor 0.7 is chosen so that the gray and nongray formulas give the same κ at high temperature ($T \gg T_{\text{Debye}}$) when grain boundary scattering dominates [11]. As the nongray model only affects heat conduction for low-frequency phonons at low temperature below 100 K and has minimal effect on our results above 80 K, we only consider nongray grain boundary scattering with the BvK dispersion relation.

For our annealed nc-Si, we have $D_{\text{avg}} = 9.7$ nm. We use the same values of A_1 , B_1 , and B_2 as those by Wang *et al.* for both Debye and BvK dispersions [11]. As MC dispersion resembles that of BvK, we use the same set of parameters for MC as for BvK. The values of A_1 , B_1 , and B_2 and our fitting parameter α are listed in Table I. The computed κ for the four models is compared with the experimental results of annealed nc-Si in Fig. 3(a). As expected, both BvK and MC models better describe the temperature dependence of our experimental results than the Debye model. The difference between gray and nongray grain boundary scattering is minor given the temperature range of this paper. It is not clear, however, why the measured κ rises with increasing temperature stronger than any model prediction. It is possible that both BvK and MC underestimate the contribution of high-frequency phonons by

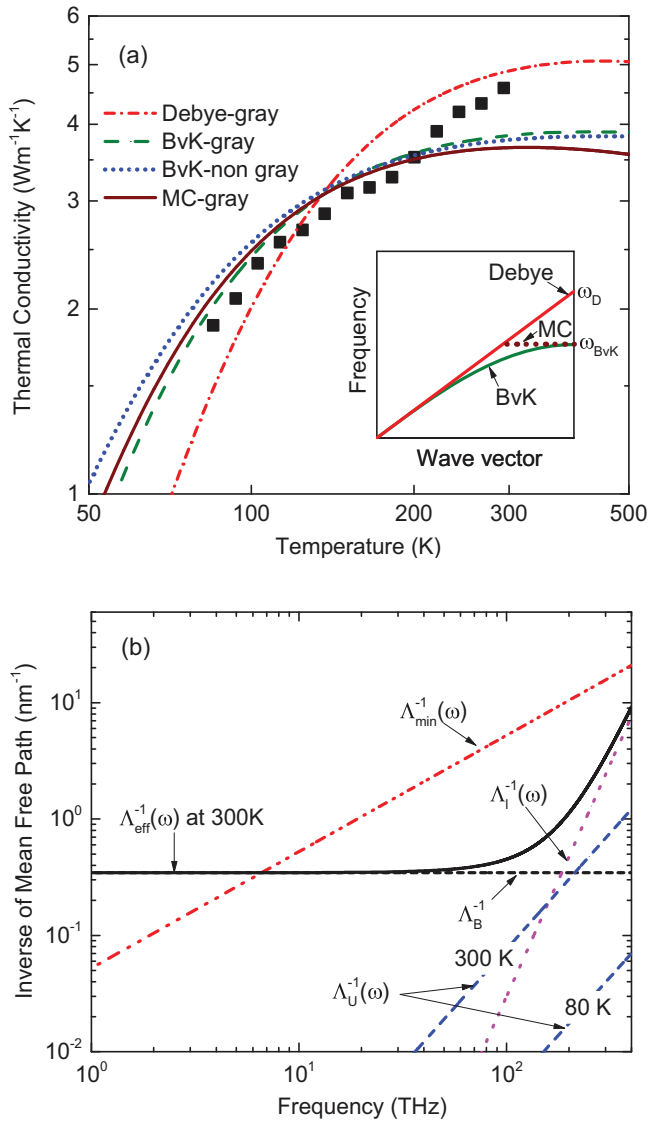


FIG. 3. (a) Thermal conductivity vs temperature of the annealed HWCVD nc-Si film, solid square, is shown with numerical models of three dispersion relation models: Debye, Born-von Karman (BvK), and Morelli-Callaway (MC), illustrated in the inset. Frequency independent (gray) grain boundary scattering is used for all three models, except for the BvK model, where frequency dependent (nongray) grain boundary scattering is also used for comparison. (b) Inverse effective phonon mean free path with its three constituents vs frequency using a grain size of 9.7 nm and parameters for “Debye-gray” from Table I. Also shown is the inverse phonon mean free path for minimum thermal conductivity.

TABLE I. Fitting parameters of several phonon scattering mechanisms, A_1 , B_1 , B_2 , and α , used in the three phonon dispersion models.

| Model | A_1 (10^{-45} s^3) | B_1 (10^{-19} s/K) | B_2 (K) | α (dimensionless) |
|-------------|-------------------------------------|-------------------------------------|--------------|-----------------------------|
| Debye-gray | 1.81 | 2.69 | 167 | 0.30 |
| BvK-gray | 1.69 | 1.53 | 140 | 0.58 |
| BvK-nongray | 1.69 | 1.53 | 140 | 0.55 |
| MC-gray | 1.69 | 1.53 | 140 | 0.80 |

reducing their group velocity too much. Higher-temperature measurements would help to show how far this trend could continue. Nevertheless, using the BvK dispersion relation and gray grain boundary scattering as an example, we demonstrate in Fig. 2(b) that κ of nc-Si with grain sizes from 550 to 9.7 nm can be described by a single set of parameters. The only grain size dependent parameter is α .

Wang *et al.* found that α for Debye is about half that of BvK for grains of 76 nm and larger [11]; we find that it is still true for our film with grain size of 9.7 nm. This is because the Debye dispersion overestimates the contribution of high-frequency phonons; α is reduced to compensate for this impact. It is interesting to note that the α we obtained by least-squares fitting of both Debye and BvK models is about 70% of those used by Wang *et al.* Note that Wang *et al.* also found that α is smaller for grain sizes of 76 and 144 nm than for 550 nm. It is possible that the Λ_B dependence on D_{avg} is stronger than linear, and a reduction of α compensates for the more rapid reduction of κ with grain size not considered in models discussed above. Possible reasons for such a stronger grain size dependence include a reduction of intragrain thermal conductivity with grain sizes. It is also interesting to note that our α for MC dispersion is similar to that used by Feser *et al.* for nanocrystalline CdSe with grain sizes between 3 and 6 nm, where grain boundary scattering dominates [26]. However, we believe that the reason for a relatively large α in the MC model in comparison to the BvK is a more aggressive reduction of $v(\omega)$ of high-frequency phonons.

To demonstrate relative contribution of each scattering mechanism that constitutes $\Lambda_{\text{eff}}^{-1}(\omega, T)$, we show the inverse MFP expressed in Eq. (9) in Fig. 3(b). In order to compare $\Lambda_{\text{eff}}^{-1}(\omega, T)$ with $\Lambda_{\text{min}}^{-1} = \omega/\pi v_s$, which determines κ_{min} , we use those parameters from Debye-gray listed in Table I. Several observations or speculations can be made. At $D_{\text{avg}} = 9.7 \text{ nm}$, $\Lambda_B^{-1}(\omega)$ dominates the phonon scattering. $\Lambda_I^{-1}(\omega)$ and $\Lambda_U^{-1}(\omega, T)$ become important at high frequency and/or high temperature. At the low frequency side, $\Lambda_{\text{eff}}^{-1}(\omega, T)$ and $\Lambda_{\text{min}}^{-1}$ cross each other at $\omega/2\pi \approx 7 \text{ THz}$. With decreasing D_{avg} , the crossover frequency increases. As it is not possible for propagating modes to have $\Lambda_{\text{eff}}^{-1}(\omega, T) > \Lambda_{\text{min}}^{-1}$, $\Lambda_{\text{eff}}^{-1}(\omega, T)$ should be replaced by $\Lambda_{\text{min}}^{-1}$ in Eq. (9) when it happens. Consequently, with decreasing D_{avg} , the percentage of propagating modes decreases, and κ may become similar for nc-Si and *a*-Si. It would be interesting to understand if and when the vibration modes in nc-Si and *a*-Si would also become similar. Theory work using molecular-dynamics simulations shows that the vibrations that carry most of the heat in small grains ($\leq 3 \text{ nm}$) nc-Si are already indistinguishable in nature to those in *a*-Si [19]. Interestingly, Braun *et al.* used the Debye dispersion relation and the exact same scattering terms as shown in Eq. (9) with almost identical A_1 , B_1 , B_2 to describe thickness dependent κ in *a*-Si, where D_{avg} is the film thickness and $\alpha = 0.5$ [7]. So the grain size in nc-Si may have played a similar role in limiting the propagator’s transport to the thickness of thin-film *a*-Si.

An empirical effective thermal conductivity (ETC) model has been proposed to predict κ of nanocrystalline materials [46]. For a given temperature, κ of nanocrystalline material depends on single-crystal thermal conductivity, single-crystal

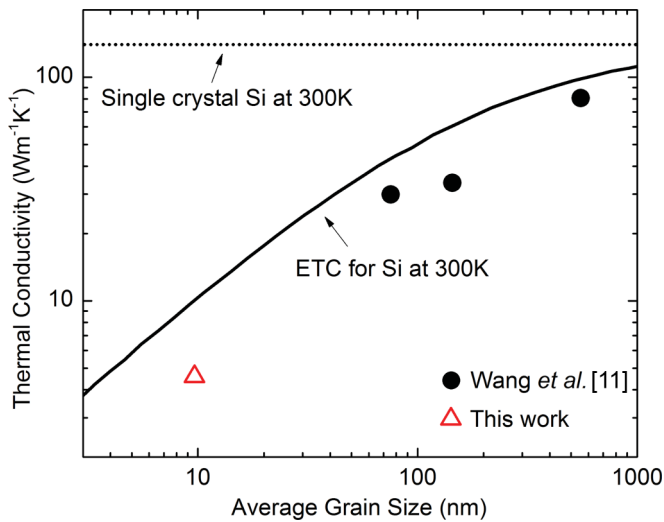


FIG. 4. Room-temperature thermal conductivity of nanocrystalline silicon as a function of average grain size for this paper and that from Ref. [11]. The solid curve is the effective thermal conductivity (ETC) explained in the text [46].

phonon MFP, and the Kaptiza thermal resistance in addition to the average grain size. The decrease of κ with decreasing grain size is modeled as a result of decreasing intragrain thermal conductance and increasing grain boundary scattering. As shown in Fig. 4, the ETC model underestimates the effect of grain size for all grain sizes from our annealed 9.7-nm nc-Si to those up to 550 nm in Ref. [11], suggesting an even stronger grain size dependence may be required.

It is known that porosity has a significant effect on heat conduction in silicon [47]. Structural analyses of similarly prepared HWCVD nc-Si films show that as-grown nc-Si has a flotation density deficiency of 8% compared to that of single crystal Si and 3–5% voids in volume [36]. It is not clear how annealing affects these voids. According to the model given by Gesele *et al.* [47], the impact of porosity on κ of crystalline silicon can be approximated by a prefactor, which is neither frequency nor temperature dependent. For a given porosity of p , the effective thermal conductivity is given by $\kappa_{\text{eff}} = (1 - p)^3 \kappa$. Assuming our annealed nc-Si has a maximum porosity

of 5%, κ would be reduced by $\sim 14\%$ and the values of α in Table I would be adjusted 14% upward accordingly. However, Wang *et al.* found that 3% porosity can cause 20% thermal conductivity reduction at room temperature [11]. This amount of reduction is more than any theoretical predictions that we are aware of. Clearly, more study is needed to understand the effect of porosity. In the meantime, we expect no major change to our above discussions would result from taking porosity into account.

V. CONCLUSION

We find that the BvK dispersion model with grain boundary scattering used by Wang *et al.* can be extended to explain κ of nc-Si with grain sizes in the ~ 10 nm range [11]. However, this is achieved by varying the prefactor of the grain boundary scattering term, α . This suggests that the inverse linear dependence of grain boundary scattering to grain size is not enough to provide a sufficient description of κ of nanocrystalline materials. A stronger dependence than linear may be needed. It is also possible that grain sizes induce further changes to the phonon density of states or dispersion relation that have not been taken into account. These changes may have played a role in determining heat conduction in nanocrystalline materials as the average grain size shrinks into the sub-10-nm region. The similarity in κ of *a*-Si and nc-Si, both in magnitude and temperature dependence, may tell us that their heat conduction mechanisms may not be as dissimilar as we currently think. After all, phonon MFP cannot be reduced to less than half of the phonon wavelength required by κ_{min} [24]. Recent theory work shows that, in solids in which nonpropagating vibration modes dominate, heat may be conducted in a fundamentally different way than what can be described by the phonon gas model [33]. More accurate atomistic modeling that considers realistic phonon dispersion and phonon density of states in nanocrystalline materials may be required to understand their thermal conduction.

ACKNOWLEDGMENTS

This work is supported by the Office of Naval Research.

- [1] L. Wiczorek, H. J. Goldsmid, and G. L. Paul, in *Thermal Conductivity 20*, edited by D. P. H. Hasselman and J. R. Thomas (Plenum, New York, 1989), p. 235.
- [2] D. G. Cahill, M. Katiyar, and J. R. Abelson, *Phys. Rev. B* **50**, 6077 (1994).
- [3] B. L. Zink, R. Pietri, and F. Hellman, *Phys. Rev. Lett.* **96**, 055902 (2006).
- [4] X. Liu, J. Feldman, D. Cahill, R. Crandall, N. Bernstein, D. Photiadis, M. Mehl, and D. Papaconstantopoulos, *Phys. Rev. Lett.* **102**, 035901 (2009).
- [5] H.-S. Yang, D. G. Cahill, X. Liu, J. L. Feldman, R. S. Crandall, B. A. Sperling, and J. R. Abelson, *Phys. Rev. B* **81**, 104203 (2010).
- [6] K. T. Regner, D. P. Sellan, Z. Su, C. H. Amon, A. J. H. McGaughey, and J. A. Malen, *Nat. Commun.* **4**, 1640 EP (2013).
- [7] J. L. Braun, C. H. Baker, A. Giri, M. Elahi, K. Artyushkova, T. E. Beechem, P. M. Norris, Z. C. Leseman, J. T. Gaskins, and P. E. Hopkins, *Phys. Rev. B* **93**, 140201 (2016).
- [8] S. Kwon, J. Zheng, M. C. Wingert, S. Cui, and R. Chen, *ACS Nano* **11**, 2470 (2017).
- [9] S. Uma, A. D. McConnell, M. Asheghi, K. Kurabayashi, and K. E. Goodson, *Int. J. Thermophys.* **22**, 605 (2001).
- [10] S. K. Bux, R. G. Blair, P. K. Gogna, H. Lee, G. Chen, M. S. Dresselhaus, R. B. Kaner, and J.-P. Fleurial, *Adv. Funct. Mater.* **19**, 2445 (2009).
- [11] Z. Wang, J. E. Alaniz, W. Jang, J. E. Garay, and C. Dames, *Nano Lett.* **11**, 2206 (2011).
- [12] P. B. Allen and J. L. Feldman, *Phys. Rev. Lett.* **62**, 645 (1989).
- [13] Y. H. Lee, R. Biswas, C. M. Soukoulis, C. Z. Wang, C. T. Chan, and K. M. Ho, *Phys. Rev. B* **43**, 6573 (1991).

- [14] J. L. Feldman, M. D. Kluge, P. B. Allen, and F. Wooten, *Phys. Rev. B* **48**, 12589 (1993).
- [15] J. L. Feldman, P. B. Allen, and S. R. Bickham, *Phys. Rev. B* **59**, 3551 (1999).
- [16] Y. He, D. Donadio, and G. Galli, *Appl. Phys. Lett.* **98**, 144101 (2011).
- [17] J. M. Larkin and A. J. H. McGaughey, *Phys. Rev. B* **89**, 144303 (2014).
- [18] W. Lv and A. Henry, *New J. Phys.* **18**, 013028 (2016).
- [19] A. Bodapati, P. K. Schelling, S. R. Phillpot, and P. Keblinski, *Phys. Rev. B* **74**, 245207 (2006).
- [20] M. Maldovan, *J. Appl. Phys.* **110**, 114310 (2011).
- [21] S. Ju and X. Liang, *J. Appl. Phys.* **112**, 064305 (2012).
- [22] T. Damart, V. M. Giordano, and A. Tanguy, *Phys. Rev. B* **92**, 094201 (2015).
- [23] A. Shah, J. Meier, E. Vallat-Sauvain, N. Wyrsh, U. Kroll, C. Droz, and U. Graf, *Solar Energy Materials and Solar Cells* **78**, 469 (2003).
- [24] D. G. Cahill, H. E. Fisher, T. Klitsner, and E. T. Swartz, *J. Vac. Sci. Technol. A* **7**, 1259 (1989).
- [25] C. Chiriac, D. G. Cahill, N. Nguyen, D. Johnson, A. Bodapati, P. Keblinski, and P. Zschack, *Science* **315**, 351 (2007).
- [26] J. P. Feser, E. M. Chan, A. Majumdar, R. A. Segalman, and J. J. Urban, *Nano Lett.* **13**, 2122 (2013).
- [27] G. Pernot, M. Stoffel, I. Savic, F. Pezzoli, P. Chen, G. Savelli, A. Jacquot, J. Schumann, U. Denker, I. Mnch, C. Deneke, O. G. Schmidt, J. M. Rampnoux, S. Wang, M. Plissonnier, A. Rastelli, S. Dilhaire, and N. Mingo, *Nat. Mater.* **9**, 491 (2010).
- [28] R. Basu, S. Bhattacharya, R. Bhatt, M. Roy, S. Ahmad, A. Singh, M. Navaneethan, Y. Hayakawa, D. K. Aswal, and S. K. Gupta, *J. Mater. Chem. A* **2**, 6922 (2014).
- [29] W. Kim, J. Zide, A. Gossard, D. Klenov, S. Stemmer, A. Shakouri, and A. Majumdar, *Phys. Rev. Lett.* **96**, 045901 (2006).
- [30] N. Mingo, D. Hauser, N. P. Kobayashi, M. Plissonnier, and A. Shakouri, *Nano Lett.* **9**, 711 (2009).
- [31] H. Zhang and A. J. Minnich, *Sci. Rep.* **5**, 8995 EP (2015).
- [32] N. Neophytou, X. Zianni, H. Kosina, S. Frabboni, B. Lorenzi, and D. Narducci, *Nanotechnology* **24**, 205402 (2013).
- [33] W. Lv and A. Henry, *Sci. Rep.* **6**, 37675 (2016).
- [34] G. Yue, J. D. Lorentzen, J. Lin, D. Han, and Q. Wang, *Appl. Phys. Lett.* **75**, 492 (1999).
- [35] D. Han, G. Yue, J. Lorentzen, J. Lin, H. Habuchi, and Q. Wang, *J. Appl. Phys.* **87**, 1882 (2000).
- [36] D. Williamson, *Sol. Energy Mater. Sol. Cells* **78**, 41 (2003).
- [37] X. Liu, C. Spiel, R. Merithew, R. Pohl, B. Nelson, Q. Wang, and R. Crandall, *Mater. Sci. Eng. A* **442**, 307 (2006).
- [38] E. Bustarret, M. A. Hachicha, and M. Brunel, *Appl. Phys. Lett.* **52**, 1675 (1988).
- [39] G. Olson and J. Roth, *Mater. Sci. Rep.* **3**, 1 (1988).
- [40] S. M. Lee and D. G. Cahill, *J. Appl. Phys.* **81**, 2590 (1997).
- [41] T. Klitsner and R. O. Pohl, *Phys. Rev. B* **36**, 6551 (1987).
- [42] X. Liu, B. E. White, Jr., R. O. Pohl, E. Iwanizcko, K. M. Jones, A. H. Mahan, B. N. Nelson, R. S. Crandall, and S. Veprek, *Phys. Rev. Lett.* **78**, 4418 (1997).
- [43] X. Liu, D. R. Queen, T. H. Metcalf, J. E. Karel, and F. Hellman, *Phys. Rev. Lett.* **113**, 025503 (2014).
- [44] C. Dames and G. Chen, *J. Appl. Phys.* **95**, 682 (2004).
- [45] S. Wei and M. Y. Chou, *Phys. Rev. B* **50**, 2221 (1994).
- [46] H. Dong, B. Wen, and R. Melnik, *Sci. Rep.* **4**, 7037 (2014).
- [47] G. Gesele, J. Linsmeier, V. Drach, J. Fricke, and R. Arens-Fischer, *J. Phys. D* **30**, 2911 (1997).